Endocrine Pathology (2025) 36:39
https://doi.org/10.1007/s12022-025-09886-9

RESEARCH

Digital Immunophenotyping of Lung Atypical Carcinoids and Large Cell Neuroendocrine Carcinomas Identifies Three Subtypes With Specific Tumor-Immune Microenvironment Features

Giovanni Centonze[1,2] · Patrick Maisonneuve[3] · Émilie Mathian[4] · Federica Grillo[5] · Giovanna Sabella[1] · Vincenzo Lagano[1] · Alessandro Mangogna[6] · Sara Pusceddu[7] · Paola Bossi[8] · Paola Spaggiari[8] · Alessandro Del Gobbo[9] · Stefano Ferrero[9] · Luigi Rolli[10] · Ugo Pastorino[10] · Luisa Bercich[11] · Andrea Tironi[11] · Mauro Roberto Benvenuti[12] · Maria Sole Gallazzi[12] · Rosalia Romano[12] · Alfredo Berruti[13] · Luca Roz[14] · Carlo Capella[15] · Matthieu Foll[4] · Massimo Milione[1]

Received: 9 August 2025 / Accepted: 14 October 2025

Abstract

Atypical carcinoids (ACs) and large cell neuroendocrine carcinomas (LCNECs) are defined by the WHO as intermediate- and high-grade lung neuroendocrine neoplasms, respectively, based on morphological criteria; however, treatment strategies remain debated. Given the emerging role of the tumor microenvironment (TME) and tumor-infiltrating lymphocytes (TILs) in cancer prognosis and therapy response, this study aimed to characterize the immune landscape of ACs and LCNECs comprehensively. Immunohistochemistry for T-cell markers (CD3, CD8), immune checkpoints (PD-1, PD-L1), HLA molecules (HLA-DR, HLA-I), and fibroblasts (α-SMA) was performed on a re-evaluated cohort of 56 ACs and 104 LCNECs. Digital image analysis quantified intra-tumor (iTILs) and stromal (sTILs) CD3 and CD8 TILs in the whole slide and in specific tumor regions (invasive margin [IM] and central tumor [CT]). LCNECs exhibited significantly higher stromal T-cell infiltration, immune checkpoint expression, and HLA compared to ACs ($p < 0.001$), while α-SMA was more prominent in ACs. No ACs showed PD-L1 tumor expression. Digital quantification confirmed greater iTILs and sTILs in LCNECs across all regions, with moderate concordance to manual counts. Interestingly, TIL parameters were higher at the IM than in the CT ($p < 0.001$). Using Boruta feature selection algorithm, Principal Component Analysis and Hierarchical Clustering, three patient clusters were identified: Cluster 1 (mainly ACs, low TILs, favorable prognosis), Cluster 2 (mixed histology, intermediate TILs, moderate prognosis), and Cluster 3 (mostly LCNECs, high TILs, poor prognosis), with distinct TME marker profiles. PD-L1 tumor expression was strongly linked to Cluster 3. These findings suggest that ACs and LCNECs may be stratified into three distinct immune clusters, highlighting the heterogeneity of their tumor microenvironment and providing a rationale for further translational studies.

Keywords Atypical carcinoid · Large cell neuroendocrine carcinomas · Tumor-infiltrating lymphocyte · Tumor microenvironment · Digital immunophenotyping · Immune clustering

Introduction

Lung neuroendocrine neoplasms (LNENs) encompass a spectrum of malignancies that include low-grade typical carcinoids (TC), intermediate-grade atypical carcinoids (AC), and high-grade neuroendocrine carcinomas, including large cell neuroendocrine carcinomas (LCNEC) and small cell lung carcinoma (SCLC) [1]. Accurate diagnosis of these diseases is critical for appropriate prognosis and clinical management. AC and LCNEC, positioned at the center of this spectrum, are classified, according to the World Health Organization (WHO), as intermediate- and high-grade neoplasms, respectively, based on morphological and histological criteria [2]. Treatment strategies and prognostic models for AC and LCNEC, unfortunately, remain controversial and poorly standardized, with overlapping features complicating their management.

In particular, while TCs are often localized carcinoids eligible for surgery as first choice, and SCLCs are

Extended author information available on the last page of the article

characterized by an initially good response rate to platinum-etoposide chemotherapy, ACs and LCNECs require a multidisciplinary approach due to their high metastatic risk and limited efficacy of chemotherapy [3, 4]. To date, due to their rarity and biological heterogeneity, no adjuvant therapy is recommended despite a high recurrence rate for ACs, and no standard treatment regimen exists for LCNECs [5–7]. Indeed, the latter are often treated using treatment recommendations extrapolated from guidelines for managing SCLC and non-small cell lung cancer (NSCLC) [4, 6]. Their rarity and heterogeneity further complicate their differential diagnosis, as no consensus has yet been reached on the optimal diagnostic approach [8, 9].

In recent years, high-throughput analyses have allowed the stratification of histological variants and the identification of novel molecular subgroups with distinct genomic signatures [10, 11]. Increasingly, ACs and LCNECs are recognized as borderline entities with molecular and morphological characteristics that blur their classification boundaries [12–14]. Growing evidence suggests the existence of an aggressive subset of lung carcinoids that share molecular features with high-grade neuroendocrine neoplasms, reinforcing the notion of a biological continuum between these tumor types [15, 16]. Therefore, these two entities may share similarities and differences rooted in distinct biological and molecular mechanisms, including tumor microenvironment and immune interactions, which could impact their classification, prognosis, and clinical management.

The tumor microenvironment (TME), which comprises immune cells, stromal cells, vasculature, and signaling molecules, plays a critical role in tumor progression, immune escape, and response to therapy [17, 18]. Tumor-infiltrating lymphocytes (TILs) have emerged as significant prognostic and predictive biomarkers across multiple tumor types, reflecting the immune landscape's activity [19, 20]. In neuroendocrine neoplasms (NENs), particularly gastro-entero-pancreatic NENs, components of the TME and inflammatory markers such as HLA, CD3, CD8, and PD-1/PD-L1, have been increasingly recognized for their prognostic and predictive significance, highlighting their potential clinical relevance [21–25]. Also, in LNENs, PD-L1 expression has been associated with necrosis, high pathologic grade, and histologic type, while CD8 + TILs demonstrated significant prognostic value [26]. Moreover, a recent study by Niedra et al. showed that tumor and α-SMA–expressing stromal cells in pancreatic neuroendocrine tumors display distinct RNA profiles depending on tumor grade [27]. Despite these insights, the composition and spatial distribution of TILs, immune checkpoint molecules, HLA, and stromal elements in ACs and LCNECs remain largely unexplored. To address this gap, the present study comprehensively investigated T-cell markers (CD3, CD8), immune checkpoints (PD-1, PD-L1), HLA molecules (HLA-I, HLA-DR), and stromal fibroblast (α-SMA).

Materials and Methods

Case Selection and Histological Review

This study is based on a multicentric, pathologically re-evaluated series of LNENs, comprising 58 ACs and 111 LCNECs, collected from our previously published studies [14, 28].

For LCNECs, a total of 148 cases were initially identified from the surgical pathology and clinical databases of five Italian institutions (Fondazione IRCCS Istituto Nazionale dei Tumori – INT, Milan; ASST Spedali Civili di Brescia – Brescia; Fondazione IRCCS Ca' Granda Ospedale Maggiore Policlinico – Milan; Ospedale Policlinico Ospedale San Martino – Genoa; and Humanitas Research Hospital – HRH, Rozzano), between 1975 and 2016 [14]. After central and blinded pathological review, and exclusion of biopsy-only material and cases with only small-cell morphology, 111 LCNECs were retained [14].

For carcinoids, 370 candidate cases were retrieved from the databases of two institutions (Fondazione IRCCS Istituto Nazionale dei Tumori—INT, Milan and ASST Spedali Civili di Brescia– Brescia) between 1988 and 2018. Following the same centralized review and predefined exclusion criteria (lack of surgical resection, biopsy-only specimens, tumors with poorly differentiated components, or uncertain primary origin), 58 ACs were included [28].

In all cases, patients' charts and tumor morphology were centrally and blindly reviewed by two expert pathologists (C.C. and M.M.) according to the latest WHO classification criteria [14, 28]. Specifically, tumor identification and subtype characterization were performed through the parallel evaluation of at least four consecutive sections from representative formalin-fixed paraffin-embedded (FFPE) tissue blocks, stained with hematoxylin–eosin (H&E), synaptophysin (Syn), chromogranin A (CgA), and Ki-67. Histological assessment included a detailed analysis of tumor architecture, necrosis, mitotic index, and cellular atypia to confirm the initial diagnoses. To determine the suitability of cases for TME immunohistochemical (IHC) analysis, all 111 LCNECs and 58 ACs FFPE blocks were reviewed, and cases with insufficient material for immunoassay were excluded.

The study was performed according to the clinical standards of the 1975 and 1983 Declaration of Helsinki and was approved by the Ethics Committee of Fondazione IRCCS INT (No. INT 171/16).

Immunohistochemistry and TME Markers

The IHC study included detection of the following markers: T cells (CD3, CD8), immune suppression (PD-L1, PD-1), HLA (HLA-DR, HLA-I), and fibroblasts (α-SMA) using the antibodies detailed in Supplementary Table 1.

To characterize the immune infiltration and the broader TME landscape, all markers were assessed in the stroma cells within (intra-tumoral) and at a distance (extra-tumoral) from the tumor. PD-L1,HLA-DR, and HLA-I were also evaluated in neoplastic cells. To ensure consistency and minimize interobserver variability, IHC staining results were independently evaluated by two expert pathologists (M.M and C.C.). For all the markers, quantification (both intra-tumoral and extra-tumoral) was based on cell densities in an area of $1mm^2$ (cells/1 mm^2), counted in areas of strongest labelling ("hot spots"). Exceptions included α-SMA, which was evaluated as the percentage of positive cells rather than cell density. Tumor marker evaluation was performed as follows: PD-L1 tumor expression was assessed according to the tumor proportion score (TPS), which categorizes expression into three levels: negative 0%, 1–49%, and ≥ 50% [29]. HLA-DR and HLA-I tumor expression was assessed using the H-score system (range 0–300), which quantifies staining intensity and the proportion of positive tumor cells. The H-score was calculated by assigning reactivity scores to tumor cells as follows: negative (0), slightly positive (1 +), moderately positive (2 +), and strongly positive (3 +). The final score ranged from 0 (all tumor cells negative) to 300 (all tumor cells strongly positive) [30].

Digital Pathology and Image Analysis

Digital slides of CD3 and CD8 IHC-stained sections were acquired using Aperio ScanScope XT® at 40 × magnification for digital pathology investigations. To analyze CD3 and CD8 tumor-infiltrating lymphocytes (TILs), considering their highly heterogeneous distribution, we conducted whole-slide image analysis. CD3 + and CD8 + TILs were quantitatively assessed, as well as their spatial distribution within the tumor microenvironment, through advanced machine-learning-based digital pathology methods.

Specifically, we tested an open-source analytic pipeline for quantifying CD3 and CD8 intratumor and/or stromal infiltrating lymphocytes from digital whole-slide images [31]. In more detail, QuPath was used for image processing [32], and for each CD3 and CD8 virtual slide, tumor areas were manually annotated by two expert pathologists. The annotated areas were then segmented into 1 mm^2 tiles, and pathologists manually distinguished the invasive margin (IM) and central tumor (CT) tiles. For each tile, an automated algorithm identified and isolated true positive lymphocyte staining, filtering out artifacts such as speckles and nonspecific background signals (Fig. 1A-B). The validated lymphocyte signals were then saved, and the image was further segmented into super-pixels, which were subsequently classified into tumor or stromal compartments using a random forest classifier trained on data implemented in R and Python. Consequently, comprehensive intratumor (iTIL) and stromal (sTIL) TILs were quantified depending upon their location within the "tumor" or "stroma" super-pixels in the entire slide (ES) and, importantly, in IM and CT (Fig. 1C). For further technical details on the analytical pipeline, please refer to the work of Yoo et al. [31].

Digital Pathology-Based Feature Selection, Clustering, and Statistical Analysis

For each patient, digital pathology analysis of CD3 and CD8 allowed the extraction of several tumor immune microenvironment (TIME) parameters [31]. Specifically, CD3 (iTIL), CD3 (sTIL), CD3 (iTIL/sTIL), CD8 (iTIL), CD8 (sTIL), CD8 (iTIL/sTIL), and tumor-stroma ratio (TSR) were quantified using four summary measures (mean, minimum, median, and maximum) and two heterogeneity metrics (coefficient of variation [CoV] and quartile deviation [QD]). CD3 and CD8 values were calculated at both the IM and CT using the four summary measures. Similarly, five different values (four summary measures plus an overall measure) were derived for the entire tumor area. A total of 207 TIME parameters were initially generated per patient (Supplementary Table 2). To reduce redundancy, we first removed variables that were highly correlated (correlation > 0.99). In addition, in order to identify the most relevant features for distinguishing WHO histology classes, we applied the Boruta feature selection algorithm, a wrapper method based on the random forest classification algorithm. Boruta is specifically designed to retain all features that contribute significantly to the predictive power of a model while eliminating irrelevant ones [33, 34]. The algorithm works by creating shuffled duplicates (shadow features) of the real features and comparing their importance scores (Z-values) obtained from the random forest model. If a real feature consistently achieves a significantly higher Z-value than the highest-ranked shadow feature across multiple independent tests, it is classified as "important" (green zone) and selected. Conversely, features that fail to outperform shadow features are marked as "unimportant" (red zone) and excluded. By applying this method, we identified a robust set of features with meaningful predictive power for WHO histology classes, optimizing model performance while minimizing noise from irrelevant variables. To further investigate the structure of the selected robust digital TIL features, we applied Principal Component Analysis (PCA), a linear dimensionality reduction technique that projects the original high-dimensional data onto a new set of orthogonal components ranked by

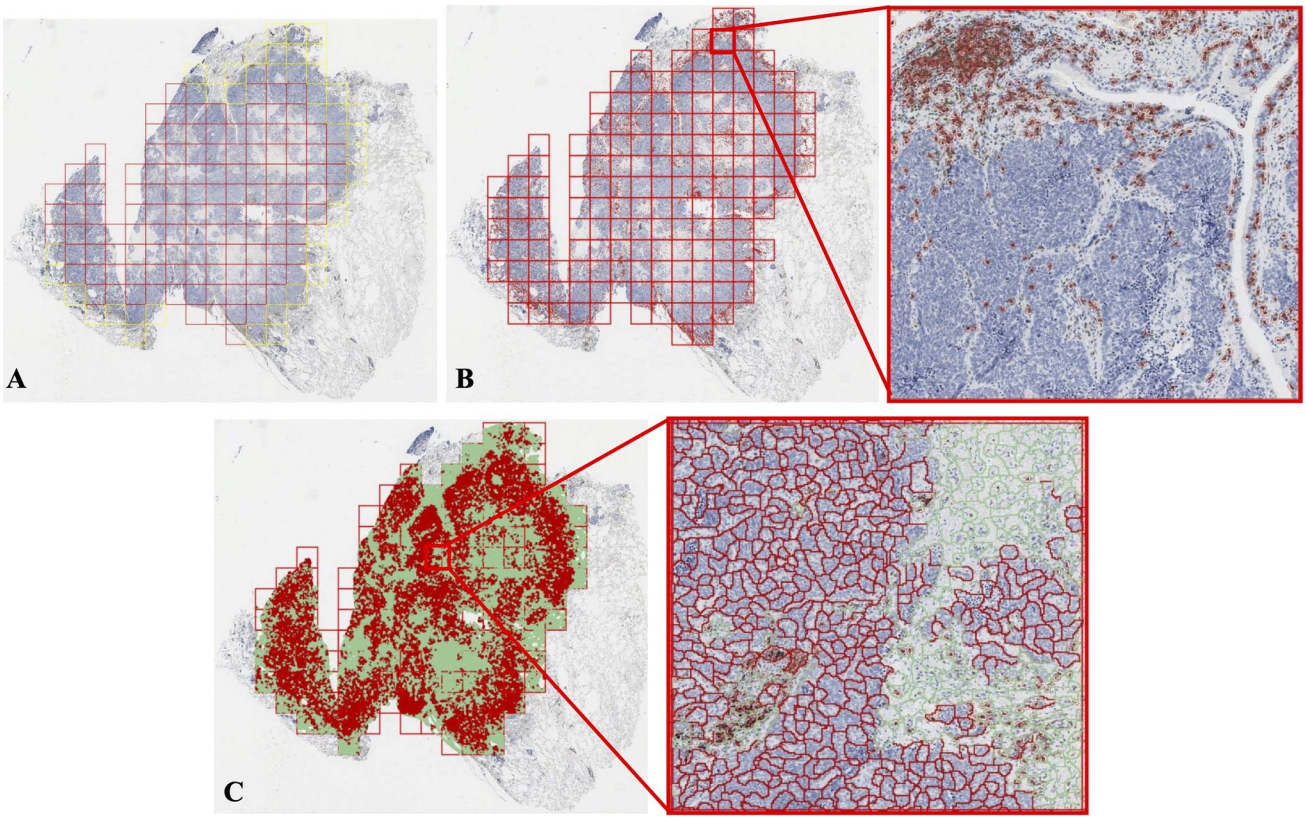

Fig. 1 **A** Annotation of tumor area with outer edges of the invasive margin marked in yellow. **B** "True" positive lymphocyte automatic quantification. **C** Tumor (red) and stroma (green) identifications with automatic quantification of intra-tumoral and stromal lymphocytes

the amount of variance they explain. Hierarchical clustering was then performed on the PCA-reduced data to identify sample groupings. This unsupervised method constructs a dendrogram based on pairwise Euclidean distances and a complete linkage criterion, progressively merging the most similar clusters.

The relationships between all intra-tumoral and extra-tumoral TME features assessed by pathologists were analyzed using Spearman's correlation coefficient. Associations between demographic characteristics and clinicopathological features with histology (ACs *vs* LNECs) or Cluster (1 *vs* 2 *vs* 3) were assessed using the Fisher exact test for categorical variables and the Wilcoxon test or Kruskal–Wallis test for continuous variables. Overall survival (OS) was assessed from the date of diagnosis to the date of death for any cause. Disease-free survival (DFS) was assessed from the date of diagnosis to the date of first relapse, death, or last follow-up, whichever occurred first. OS and DFS curves were drawn using the Kaplan–Meier method. The log-rank test was used to assess the survival difference between patient groups. Pearson's correlation coefficient was used to evaluate the relationship between intra-tumoral and extra-tumoral CD3 and CD8 densities obtained through automated image analysis and the corresponding quantitative counts assessed manually by pathologists. Data analysis was performed using the R environment for statistical computing and graphics (R Foundation, Vienna, Austria- Version 4.3.3). All tests were two-sided, and p-values < 0.05 were considered statistically significant.

Results

Cohort Characteristics and TME Marker Distribution

Overall, a total of 56 ACs and 104 LCNECs had sufficient tissue for IHC analysis and were included in the study. The associations between clinico-pathological characteristics and TME marker expression, as assessed by pathologists, with WHO histology classes are summarized in Table 1. The cohort was composed of more males than females (59.4% *vs* 40.6%), with a median age of 65 years. Regarding tumor stage distribution, 58 cases (36.2%) were stage I, 35 (21.9%) stage II, 39 (24.4%) stage III, and 28 (17.5%) stage IV. Advanced-stage tumors (stage III-IV) were predominantly LCNECs, whereas ACs had the highest proportion of stage I cases. A history of smoking was more common among LCNEC patients, with former

Table 1 Clinicopathological characteristics and TME IHC expression according to WHO Class

	All patients	ACs	LCNECs	*p*-value*
Total	160(100)	56(100)	104(100)	
Female	65 (40.6)	32 (57.1)	33 (31.7)	
Male	95 (59.4)	24 (42.9)	71 (68.3)	**0.002**
Age				
Median [range]	65 [27–84]	61 [27–78]	66 [34–84]	**0.007**
Stage				
I	58 (36.2)	28 (50.0)	30 (28.8)	
II	35 (21.9)	12 (21.4)	23 (22.1)	
III	39 (24.4)	12 (21.4)	27 (26.0)	
IV	28 (17.5)	4 (7.1)	24 (23.1)	**0.02**
Smoking				
Never smoking	15 (9.4)	15 (38.2)	0 (0.0)	
Former smoking	47 (29.6)	19 (34.5)	28 (26.9)	
Current smoking	97 (61.0)	21 (27.3)	76 (73.1)	**< 0.0001**
CD3 Intra Count				
Median [range]	106 [0–1837]	40 [0–1837]	141 [10–1626]	**< 0.0001**
CD3 Extra Count				
Median [range]	858 [30–3231]	556 [30–2323]	1136 [253–3231]	**< 0.0001**
CD8 Intra Count				
Median [range]	101 [0–1697]	40 [0–1071]	152 [10–1697]	**< 0.0001**
CD8 Extra Count				
Median [range]	621 [20–4091]	399 [20–1050]	833 [162–4091]	**< 0.0001**
PD-1 Intra Count				
Median [range]	30 [0–625]	0 [0–313]	51 [0–625]	**< 0.0001**
PD-1 Extra Count				
Median [range]	343 [0–1566]	131 [0–778]	515 [0–1566]	**< 0.0001**
PD-L1 Tumor				
Negative	137 (85.6)	56 (100)	81 (77.9)	
1–49%	18 (11.3)	0 (0.0)	18 (17.3)	
≥ 50%	5 (3.1)	0 (0.0)	5 (4.9)	**< 0.0001**
PD-L1 Intra Count				
Median [range]	0 [0–576]	0 [0–131]	0 [0–576]	**< 0.0001**
PD-L1 Extra Count				
Median [range]	0 [0–1212]	0 [0–323]	1 [0–1212]	**< 0.0001**
HLA-DR Tumor H-score				
Median [range]	0 [0–300]	0 [0–60]	0 [0–300]	**0.01**
HLA-DR Intra Count				
Median [range]	121 [10–708]	207 [10–708]	101 [30–626]	**0.0005**
HLA-DR Extra Count				
Median [range]	697 [131–2831]	606 [131–1313]	843 [172–2831]	**0.0001**
HLA-I Tumor H-score				
Median [range]	75 [0–300]	90 [0–300]	55 [0–300]	0.6
HLA-I Intra Count				
Median [range]	51 [0–455]	0 [0–404]	61 [0–455]	**< 0.0001**
HLA-I Extra Count				
Median [range]	788 [30–5242]	571 [30–2050]	1086 [71–5242]	**< 0.0001**
Actin α-SMA Intra H Score				
Median [range]	180 [30–300]	270 [60–300]	150 [30–270]	**< 0.0001**
Actin α-SMA Extra H Score				
Median [range]	120 [15–270]	120 [30–270]	90 [15–270]	**0.002**

*p-value based on Fisher's exact test for categorical variables and the Wilcoxon test for continuous variables. *AC*, Atypical Carcinoid; *LCNEC*, Large Cell Neuroendocrine Carcinoma; *CD*, Cluster of Differentiation; *PD-1*, Programmed Death-1; *PD-L1*, Programmed Death-Ligand 1; *HLA*, Human Leukocyte Antigen; *α-SMA*, alpha Smooth Muscle Actin

and current smokers comprising 26.9% and 73.1% of this group, respectively. Data on adjuvant treatment were available for 86 patients of the whole cohort (53.8%). Among the 104 LCNEC patients, treatment information was available for 60 cases: 29 (48.3%) received platinum-based chemotherapy (pre- and/or postoperatively), 15 (25.0%) received combined chemoradiotherapy, 1 (1.7%) radiotherapy alone, and 15 (25.0%) did not receive any adjuvant treatment. For the 56 AC patients, treatment data were available for 26 cases: 2 (7.7%) received somatostatin analogues, 2 (7.7%) chemotherapy, 1 (3.8%) radiotherapy, 1 (3.8%) combined chemoradiotherapy, and 20 (76.9%) did not receive any treatment. The median overall survival (OS) for the entire cohort was 26 months (95% CI: 21–39), with LCNEC patients showing a median OS of 17 months (95% CI: 13–19) compared to 102 months (95% CI: 73–not reached) for AC patients.

Significant differences in TME marker expression were observed between ACs and LCNECs (Table 1). LCNECs exhibited significantly higher densities of CD3 and CD8 T cells in both the intra-and extratumoral compartments compared to ACs ($p < 0.001$). Similarly, immune checkpoint markers were more abundant in LCNECs, with significantly higher PD-1 expression in both intra-tumor and extra-tumor regions ($p < 0.001$). Notably, tumor PD-L1 positivity was exclusive to LCNECs ($p < 0.001$), and PD-L1 expression in both the intratumoral and extratumoral compartments was enriched in LCNECs compared to ACs. Furthermore, HLA-DR and HLA-I expression in extra-tumor regions was more frequent in LCNECs than in ACs ($p < 0.001$). Interestingly, while tumor HLA-DR expression was significantly higher in LCNECs, no differences were observed for tumor HLA-I expression. Lastly, ACs exhibited significantly higher α-SMA expression compared to LCNECs (p = 0.002).

CD3 and CD8 Digital Quantification and Pathologist Agreement

Digital analysis of CD3 and CD8 lymphocytes confirmed that LCNECs exhibited significantly higher densities of both iTILs and sTILs compared to ACs ($p < 0.001$) (Fig. 2A). The data was confirmed in IM and CT. Notably, iTIL and sTIL densities showed strong positive correlations with immune checkpoint markers, including both intra and extratumoral PD-1, as well as PD-L1 in the intratumoral and extratumoral compartments. Interestingly, in both ACs and LCNECs, the IM displayed significantly higher CD3 and CD8 TIL median densities than the CT ($p < 0.001$) (Fig. 2B-C).

Moderate concordance was observed between digital image analysis and the manual quantification of CD3/CD8 in both intra- and extratumoral compartments. Pearson correlation coefficients (r) between manual and digital assessments ranged from 0.62 to 0.78 ($p < 0.0001$). The highest agreement was observed for CD8 intra-tumoral quantification (r = 0.78), followed by CD3 in the extra compartment (r = 0.66), CD8 in the extra compartment (r = 0.63), and the lowest agreement for CD3 intra-tumoral quantification (r = 0.62) (Supplementary Fig. 1).

Digital Pathology-Based Feature Selection

Following the removal of highly correlated variables (correlation > 0.99), a refined set of 183 TIME parameters was obtained. Using the Boruta algorithm, feature selection identified 31 key features as the most relevant in distinguishing TIME profiles between ACs and LCNECs (Supplementary Table 3). Supplementary Fig. 2 shows the feature selection results, where variables highlighted in green represent the 31 important features, while those in red are classified as unimportant according to the Boruta algorithm. In more detail, the 31 important features included CD3 and CD8 across intratumoral (iTIL) and stromal (sTIL) compartments, as

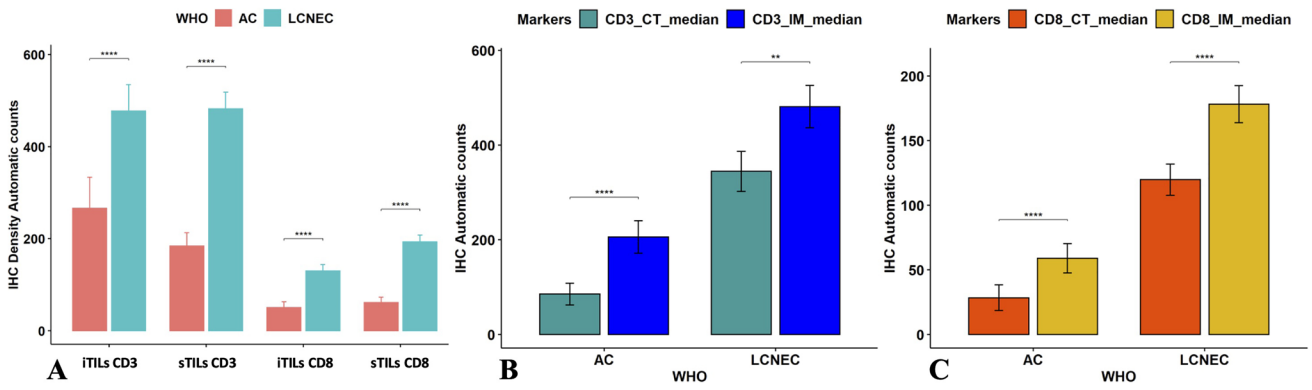

Fig. 2 **A** iTILs and sTILs bar plot in AC and LCNEC. **B** CD3 TILs in CT and IM in AC and LCNEC. **C** CD8 TILs in CT and IM in AC and LCNEC

well as their spatial distribution in the IM and CT regions. Among the selected features, CD8-related parameters were predominant, indicating the relevance of CD8 + T-cell infiltration patterns in defining distinct tumor immune environments. CD3-related features, such as CD3_CT_median and CD3_CT_median_str, were also retained, highlighting the differential T-cell infiltration dynamics in ACs and LCNECs.

Immune-Based Clustering and Clinical Relevance

Principal component analysis (PCA) was applied to the 31 key CD3 and CD8 digital features identified through the Boruta feature selection algorithm. This dimensionality reduction revealed the distribution of AC and LCNEC patients along the first two principal components, which together explain 62.06% of the total variance (Fig. 3A). Hierarchical clustering on the first four principal components, collectively explaining 79.46% of the total variance, revealed three main clusters of patients, suggestive of distinct immune microenvironment profiles and clinical characteristics (Fig. 3B-C). Separation between clusters was also evident in the PC1 *vs* PC3 and PC1 *vs* PC4 plots, supporting the robustness of the clustering structure (Supplementary Fig. 3). Notably, PC1 explained 48.83% of the total variance, indicating that the main discriminative signal lies along this axis.

An in-depth analysis of these clusters uncovered specific differences in TIL density, histology distribution, and prognostic implications (Table 2, Fig. 3D, Fig. 4A-B). Cluster 1 was predominantly composed of AC cases (39 ACs and 13 LCNECs) and was characterized by low TIL density and a more favorable prognosis. This cluster was significantly enriched for younger patients ($p = 0.011$) and also tended to be enriched for female patients compared to the other two clusters ($p = 0.12$). Additionally, non-smokers were more prevalent in Cluster 1 than in

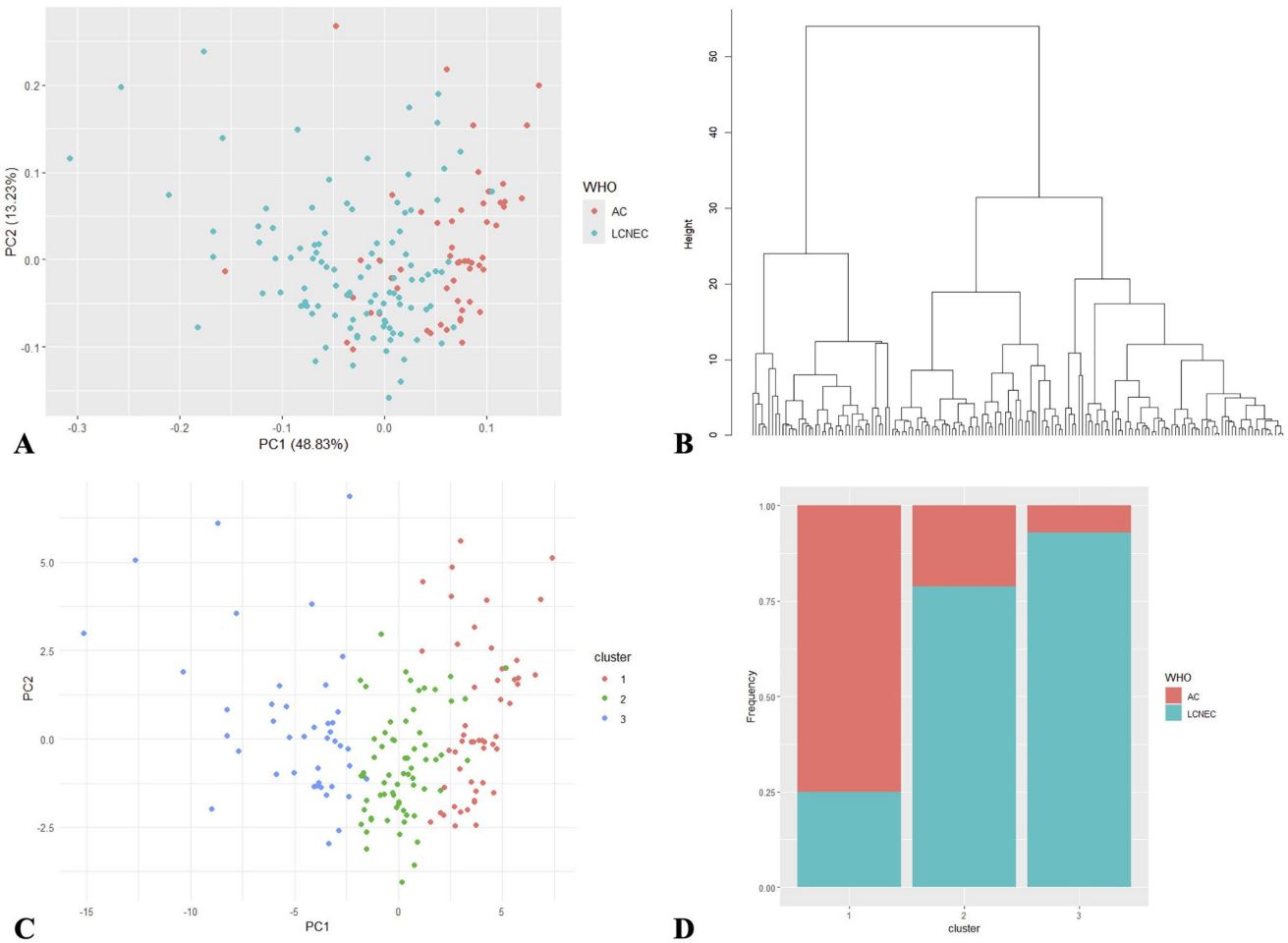

Fig. 3 **A** Principal Component Analysis (PCA) plot based on 31 robust TIL-related features, showing the distribution of AC and LCNEC samples along the first two principal components (PC1 and PC2). **B** Dendrogram generated by hierarchical clustering (Ward's method). **C** PCA plot followed by hierarchical clustering using Ward's method (3 clusters). **D** Distribution of AC and LCNEC across the three clusters

Table 2 Clinicopathological characteristics and TME IHC expression according to Cluster

	All patients	Cluster 1	Cluster 2	Cluster 3	*p*-value*	Pairwise comparisons		
						p-value# 1 *vs* 2	*p*-value# 1 *vs* 3	*p*-value# 2 *vs* 3
Total	160(100)	52(100)	66(100)	42(100)				
Gender								
Female	65 (40.6)	27 (51.9)	22 (33.3)	16 (38.1)				
Male	95 (59.4)	25 (48.1)	44 (66.7)	26 (61.9)	0.12	0.06	0.2	0.7
Age								
Median [range]	65 [27–84]	60 [29–82]	65 [27–77]	68 [45–84]	**0.011**	0.076	**0.003**	0.13
WHO Class								
AC	56 (35.0)	39 (75.0)	14 (21.2)	3 (7.1)				
LCNEC	104 (65.0)	13 (25.0)	52 (78.8)	39 (92.9)	**< 0.001**	**< 0.001**	**< 0.001**	0.061
Stage								
I	58 (36.2)	24 (46.2)	18 (27.3)	16 (38.1)				
II	35 (21.9)	14 (26.9)	15 (22.7)	6 (14.3)				
III	39 (24.4)	9 (17.3)	18 (27.3)	12 (28.6)				
IV	28 (17.5)	5 (9.6)	15 (22.7)	8 (19.0)	0.2	0.063	0.2	0.6
Smoking								
Never smoking	15 (9.4)	10 (19.6)	5 (7.6)	0 (0.0)				
Former smoking	47 (29.6)	16 (31.4)	18 (27.3)	13 (31.0)				
Current smoking	97 (61.0)	25 (49.0)	43 (65.2)	29 (69.0)	**0.016**	0.088	**0.003**	0.2
CD3 Intra Count								
Median [range]	106 [0–1837]	40 [0–737]	111 [10–586]	232 [61–1837]	**< 0.001**	**< 0.001**	**< 0.001**	**< 0.001**
CD3 Extra Count								
Median [range]	858 [30–3231]	515 [30–1687]	939 [192–2828]	1490 [404- 3231]	**< 0.001**	**< 0.001**	**< 0.001**	**< 0.001**
CD8 Intra Count								
Median [range]	101 [0–1697]	30 [0–465]	101 [20–657]	222 [61–1697]	**< 0.001**	**< 0.001**	**< 0.001**	**< 0.001**
CD8 Extra Count								
Median [range]	621 [20–4091]	318 [20–1303]	657 [162–2414]	1126 [263–4091]	**< 0.001**	**< 0.001**	**< 0.001**	**< 0.001**
PD-1 Intra Count								
Median [range]	30 [0–625]	0 [0–101]	30 [0–354]	86 [20–625]	**< 0.001**	**< 0.001**	**< 0.001**	**< 0.001**
PD-1 Extra Count								
Median [range]	343 [0–1566]	121 [0–566]	404 [30–1192]	717 [172–1566]	**< 0.001**	**< 0.001**	**< 0.001**	**< 0.001**
PD-L1 Tumor								
Negative	137 (85.6)	51 (98.1)	59 (89.4)	27 (64.3)				
1–49%	18 (11.3)	1 (1.9)	7 (10.6)	10 (23.8)				
≥ 50%	5 (3.1)	0 (0.0)	0 (0.0)	5 (11.9)	**< 0.001**	0.076	**< 0.001**	**0.001**
PD-L1 Intra Count								
Median [range]	0 [0–576]	0 [0–71]	0 [0–333]	20 [0–576]	**< 0.001**	**0.007**	**< 0.001**	**< 0.001**
PD-L1 Extra Count								
Median [range]	0 [0–1212]	0 [0–131]	0 [0–525]	136 [0–1212]	**< 0.001**	**< 0.001**	**< 0.001**	**< 0.001**
HLA-DR Tumor H-score								
Median [range]	0 [0–300]	0 [0–0]	0 [0–285]	0 [0–300]	**0.002**	**0.03**	**< 0.001**	0.076
HLA-DR Intra Count								
Median [range]	121 [10–708]	162 [10–708]	101 [40–626]	96 [30–606]	0.11	0.2	0.05	0.2
HLA-DR Extra Count								
Median [range]	697 [131–2831]	525 [131–1192]	828 [242–2707]	1020 [232–2831]	**< 0.001**	**< 0.001**	**< 0.001**	**0.032**
HLA-I Tumor H-score								
Median [range]	75 [0–300]	10 [0–300]	50 [0–300]	40 [0–300]	**0.046**	**0.013**	0.1	0.6

Table 2 (continued)

	All patients	Cluster 1	Cluster 2	Cluster 3	*p*-value*	Pairwise comparisons		
						p-value# 1 *vs* 2	*p*-value# 1 *vs* 3	*p*-value# 2 *vs* 3
HLA-I Intra Count								
Median [range]	51 [0–455]	0 [0–404]	61 [0–414]	91 [0–455]	**< 0.001**	**< 0.001**	**< 0.001**	0.13
HLA-I Extra Count								
Median [range]	788 [30–5242]	525 [30–1252]	990 [71–3838]	1546 [71–5242]	**< 0.001**	**< 0.001**	**< 0.001**	**0.004**
Actin α-SMA Intra H-score								
Median [range]	180 [30–300]	263 [75–300]	150 [30–300]	135 [30–270]	**< 0.001**	**< 0.001**	**< 0.001**	**0.025**
Actin α-SMA Extra H-score								
Median [range]	120 [15–270]	120 [30–240]	120 [15–270]	90 [15–180]	**0.002**	**0.021**	**< 0.001**	0.14

p-value based on Fisher's exact test for categorical variables and the Kruskal–Wallis test for continuous variables. #p-value based on Fisher's exact test for categorical variables and the Wilcoxon test for continuous variables. *WHO*, World Health Organization; *CD*, Cluster of Differentiation; *PD-1*, Programmed Death-1; *PD-L1*, Programmed Death-Ligand 1; *HLA*, Human Leukocyte Antigen; *α-SMA*, alpha Smooth Muscle Actin

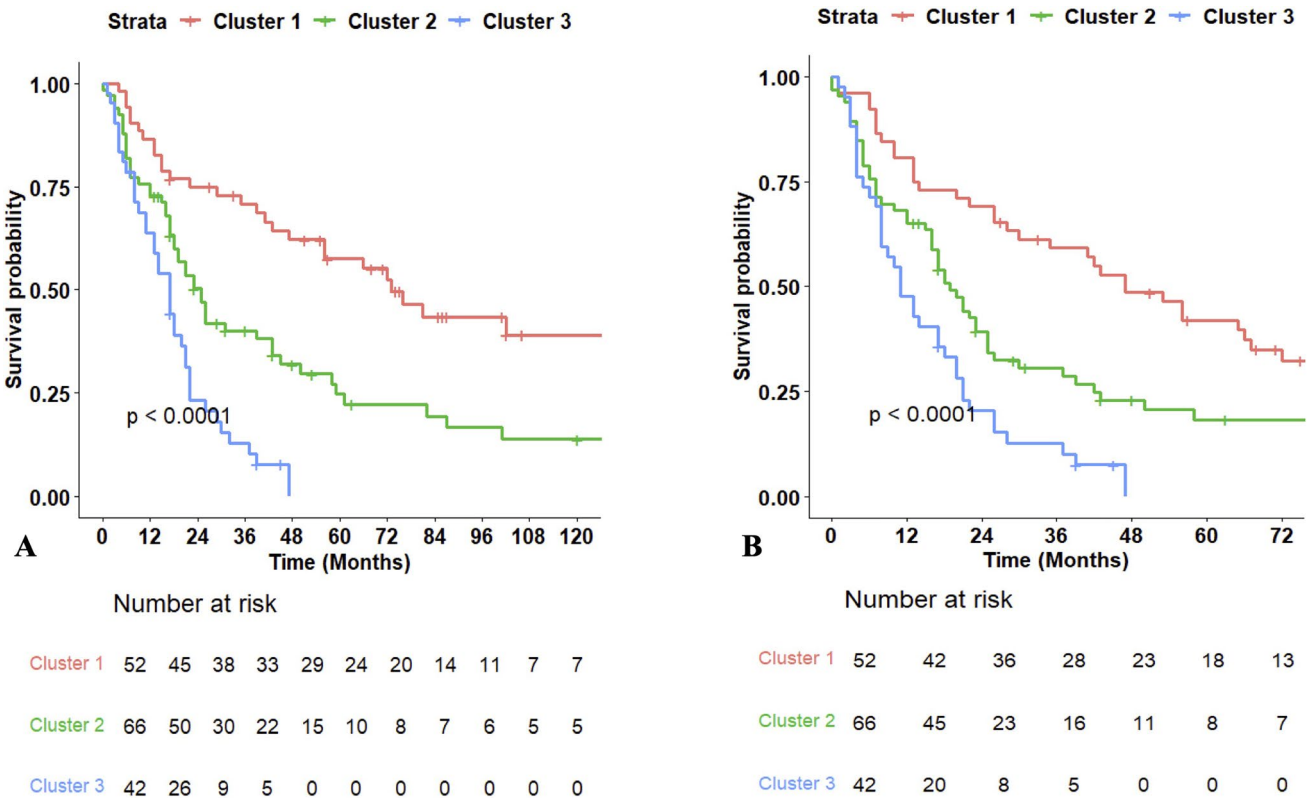

Fig. 4 **A** Overall survival and **B** disease-free survival of patients according to cluster

Clusters 2 and 3 ($p = 0.016$). Cluster 2 represented a consistent heterogeneous group, consisting of both AC (14 cases) and LCNEC (52 cases) tumors, with intermediate TIL densities and moderate prognosis. Finally, Cluster 3 was strongly enriched for LCNECs (39 LCNECs and only 3 ACs), exhibited the highest TIL densities, and was linked to the poorest prognosis (Fig. 4A-B). Notably, this cluster had the highest median age, indicating an enrichment of older individuals ($p = 0.011$). Moreover, Cluster 3 displayed a distinct TME profile, with a marked increase in TILs, HLA antigens, and immune suppression markers compared to the other clusters. Tumor PD-L1 expression was strongly associated with Cluster 3 ($p < 0.001$).

Discussion

This study provides a comprehensive analysis of the TME in a cohort of patients with lung AC and LCNEC, with a specific focus on TILs, PD-L1 expression, and other key immune markers. By integrating IHC, digital quantification, feature selection, and clustering, we identified distinct immune profiles that differentiate ACs from LCNECs and stratify patients into three different clusters. Our findings reinforce the role of CD3 + and CD8 + TILs as potential determinants of the immune landscape in neuroendocrine lung tumors and highlight the presence of an underlying immune-based activation pattern that transcends the traditional WHO classification stratification.

In short, our analysis revealed that LCNECs exhibit significantly higher densities of CD3 + and CD8 + T cells across both intratumoral and extratumoral compartments compared to ACs. The increased immune infiltration in LCNECs was accompanied by a higher expression of immune checkpoint markers, particularly PD-1 and PD-L1, with PD-L1 tumor expression being exclusively detected in LCNECs. In addition, HLA molecules were generally more frequently expressed in LCNECs than in ACs, further supporting the notion of a more immunologically active TME in LCNECs. Overall, these findings are consistent with previous studies suggesting that high-grade neuroendocrine lung carcinomas tend to be more immunoreactive than lower-grade neuroendocrine tumors. In more detail, Ferencz et al. [35], using a panel of 15 immune-related markers, demonstrated that SCLC and LCNEC tumors exhibit a more immunogenic phenotype than ACs. In line with our findings, their study indicated that high CD8 + T-cell infiltration tended to be a negative prognostic factor. However, these result contrasts with the findings of Wang et al. [26], who reported that increased CD8 + TIL density was associated with improved PFS and OS in LNEN patients. A possible explanation for this discrepancy may relate to differences in study design and methodology, as Wang et al. evaluated prognosis in a relatively small subset of ACs (n = 2) and LCNECs (n = 28), and survival analyses were based on a median dichotomization of CD8 + TIL density [26].

Different studies have reported a complete absence of PD-L1 expression in AC, further reinforcing the idea that high-grade NECs possess a more active immune microenvironment [36, 37]. In addition, Kasajima et al. reported that NECs exhibited more tumor-associated inflammation than carcinoids, in which both inflammatory and tumor cells lacked PD-L1 expression [38]. They concluded that anti-tumor inflammation was virtually absent in carcinoids and likely played no significant role in their biology. On the other hand, in our series, higher α-SMA expression observed in ACs may reflect a stronger stromal-driven biology, in contrast to the more immune-infiltrated profile of LCNECs. Collectively, these findings suggest that the substantial presence of CD8 + TILs and PD-L1 expression in LCNECs may indicate a greater responsiveness to immune checkpoint inhibitors, whereas the immune-desert phenotype of carcinoids reflects a fundamentally distinct tumor-microenvironment interaction, potentially limiting their benefit from immunotherapy.

Digital pathology and machine learning approaches allowed for an automatic assessment of CD3 + and CD8 + TIL distribution with moderate concordance between digital quantification and pathologist assessments. Boruta-based feature selection identified 31 key features, with CD8-related parameters predominating, highlighting the central role of CD8 + T-cell infiltration in defining immune microenvironment differences between ACs and LCNECs. Unsupervised clustering identified different immune-based patient groups with different immunological and clinical characteristics. In this context, emerging studies have identified molecularly distinct subgroups, providing a more refined prognostic classification and better predictions of therapy response. Based on genomic profiling, LCNECs have been categorized into two major subtypes: one characterized by alterations in *TP53* and *KRAS*/*STK11*/*KEAP1*, and another with concurrent *TP53* and *RB1* inactivation. Notably, George et al. reported that the latter, referred to as "LCNEC Type II," exhibited elevated expression of immune-related genes and upregulation of immune pathways, which may influence patient responses to immunotherapy [12]. In our study, LCNECs were primarily divided into two clusters, with Cluster 3 displaying the highest immune infiltration, HLA expression, and a significant enrichment in PD-1 and PD-L1 levels. This immune-inflamed phenotype cluster could potentially overlap with LCNEC Type II, further supporting the existence of biologically distinct LCNEC subtypes with potential therapeutic implications. In addition, a transcriptional study on ACs and LCNECs by Simbolo et al. revealed significant molecular and biological heterogeneity [39], suggesting that these tumors may represent three distinct molecular diseases with potential clinical relevance: an AC-enriched group driven by *MEN1* inactivation, a mixed group with intermediate molecular features, and an LCNEC-enriched group characterized by *RB1* inactivation. Supporting the concept of a molecular continuum between low- and high-grade pulmonary NENs, Alcala et al. identified a subgroup of ACs, termed "supra-carcinoids", which clustered with LCNECs in an integrative multi-omics analysis [15]. These tumors, despite displaying carcinoid-like morphology, exhibit molecular and clinical features more consistent with LCNECs. Consistent with these findings, our study identified three distinct immune TME subtypes: a predominantly AC-enriched group with low TIL density, minimal stromal

PD-L1 and HLA expression, a mixed group with intermediate TME characteristics, and an LCNEC-enriched group exhibiting the highest TIL densities, heightened immune activation, significant PD-L1 tumor expression, and the poorest prognosis. Notably, a small subset of ACs clustered within this latter LCNEC-like group, paralleling the supracarcinoid concept. Finally, the recent study by Ferencz et al. demonstrated that LNEN samples could be separated fairly well based on the immune cell expression of the immune-related markers, using unsupervised hierarchical clustering [35]. Although direct correlation with published genomic subtypes could not be assessed in our series, the observed parallels suggest that immune-based clusters may partially overlap or complement the underlying molecular heterogeneity, underscoring the need for integrative studies combining genetic and immune profiling.

Lastly, our results reinforce the growing recognition of LCNECs as heterogeneous entity within the spectrum of lung NENs. While historically managed with SCLC-based treatment regimens, emerging molecular and immune profiling studies suggest that LCNECs harbor unique actionable characteristics [4]. In this context, our analysis identifies three immune-defined subgroups, including a cluster of LCNECs with marked immune infiltration and checkpoint expression. Although these findings are not yet mature to inform clinical decisions, they highlight how immune-based classification could provide complementary information to molecular profiling, supporting efforts to refine patient stratification. An integrated approach, combining genomic and immune data, may contribute to the identification of predictive biomarkers of response to immunotherapy and guide the design of future prospective studies.

Several limitations of this study should be acknowledged. First, its retrospective design and relatively small sample size may limit the generalizability of our findings. Additionally, due to the observational nature of the study, causal relationships between TME characteristics and clinical data cannot be established. Another limitation is the limited therapeutic information, which prevented a systematic assessment of treatment effects on immune clusters and survival outcomes. Furthermore, the lack of molecular analyses is an important limitation, as these would be crucial to assess the association between immune clusters and molecular subtypes of LCNECs and ACs. Future studies incorporating comprehensive genomic profiling, complete therapeutic data, and larger prospective cohorts are needed to further validate these findings and refine the therapeutic implications of targeting the TME in pulmonary NENs.

In summary, our study provides a comprehensive TIL and immune landscape characterization of LNENs, demonstrating that ACs and LCNECs exhibit distinct TME profiles. Through digital, pathology-driven, feature selection and clustering, we identified three patient subgroups with differing TIL expression and immune infiltration patterns. These findings highlight the potential of immune-based markers in LNENs and provide a rationale for further exploring immunotherapeutic strategies in LCNECs. Future studies integrating molecular profiling with immune characterization will be essential to fully elucidate the clinical significance of these immune subtypes and optimize treatment approaches.

Supplementary Information The online version contains supplementary material available at https://doi.org/10.1007/s12022-025-09886-9.

Acknowledgements We would like to take this opportunity to thank Fabiola Monaco and Giulia Bonarini (executive secretary Fondazione IRCCS – Istituto Nazionale dei Tumori, Milan, Italy) for their effort in managing the work of all researchers involved in this study.

Author contributions Study concept and design – G.C., L.R., C.C., M.M.; Methodology – G.C., E.M., G.S., V.L., A.M., M.F., C.C., M.M.; Data analysis – G.C., P.M., E.M., M.M.; Drafting of manuscript – G.C.; Critical revision of the manuscript for important intellectual content – P.M., E.M., F.G., G.S., A.M., S.P., P.B., P.S., A.D.G., S.F., L.R., U.P., L.B., A.T., M.R.B., M.S.G., R.M., A.B., L.R., M.F., C.C., M.M.; Statistical analysis – G.C., P.M., E.M; Study supervision – M.F., C.C., M.M..

Funding This work was supported by Italian Ministry of Health (ERP-2017–23671129 "PMTR-pNET" Project to M.M.); by Fondazione IRCCS Istituto Nazionale Tumori di Milano 5 × 1,000 funds – 2014 MIUR – grant "Integrative molecular analysis of pure and combined lung large cell neuroendocrine carcinoma (LCNEC)" (Project to M.M); partially by the Italian Ministry of Health with Ricerca Corrente and 5 × 1,000 funds (Project to P.M.). Giovanni Centonze was supported by a FIRC-AIRC fellowship for Italy.

Data Availability The data that support the findings of this study are available on request from the corresponding author.

Declarations

Competing Interests The authors declare no competing interests.

Author's Note This work is dedicated to the memory of Laura Salvaterra, a courageous woman who battled against cancer and invites us to fight cancer every day in her name, even after her demise.

Conflicts of Interest The authors have disclosed that they have no significant relationships with, or financial interest in, any commercial companies pertaining to this article. Where authors are identified as personnel of the International Agency for Research on Cancer/World Health Organization, the authors alone are responsible for the views expressed in this article and they do not necessarily represent the decisions, policy or views of the International Agency for Research on Cancer/World Health Organization.

Declarations The results reported in this manuscript are original and were presented as oral platform presentation during the United States and Canadian Academy of Pathology's 112th Annual Meeting (USCAP) in New Orleans, March 11–16, 2023.

References

1. Rindi G, Mete O, Uccella Set al. Overview of the 2022 WHO Classification of Neuroendocrine Neoplasms. Endocr Pathol 33: 115–154, 2022.
2. Nicholson AG, Tsao MS, Beasley MBet al. The 2021 WHO Classification of Lung Tumors: Impact of Advances Since 2015. J Thorac Oncol 17: 362–387, 2022.
3. Caplin ME, Baudin E, Ferolla Pet al. Pulmonary neuroendocrine (carcinoid) tumors: European Neuroendocrine Tumor Society expert consensus and recommendations for best practice for typical and atypical pulmonary carcinoids. Ann Oncol 26: 1604–1620, 2015.
4. Sen T, Dotsu Y, Corbett Vet al. Pulmonary neuroendocrine neoplasms: the molecular landscape, therapeutic challenges, and diagnosis and management strategies. Lancet Oncol 26: e13–e33, 2025.
5. Fasano M, Della Corte CM, Papaccio F, Ciardiello F, Morgillo F Pulmonary Large-Cell Neuroendocrine Carcinoma: From Epidemiology to Therapy. J Thorac Oncol 10: 1133–1141, 2015;
6. Tsoukalas N, Baxevanos P, Aravantinou-Fatorou Eet al. Advances on systemic treatment for lung neuroendocrine neoplasms. Ann Transl Med 6: 146, 2018.
7. Sobash PT, Ullah A, Karim NA Survival Benefit of Adjuvant Chemotherapy in Pulmonary Carcinoid Tumors. Cancers (Basel) 14, 2022.
8. Rindi G, Klimstra DS, Abedi-Ardekani Bet al. A common classification framework for neuroendocrine neoplasms: an International Agency for Research on Cancer (IARC) and World Health Organization (WHO) expert consensus proposal. Mod Pathol 31: 1770–1786, 2018.
9. Pelosi G, Travis WD Head-to-head: Should Ki67 proliferation index be included in the formal classification of pulmonary neuroendocrine neoplasms? Histopathology 85: 535–548, 2024.
10. Rekhtman N, Pietanza MC, Hellmann MDet al. Next-Generation Sequencing of Pulmonary Large Cell Neuroendocrine Carcinoma Reveals Small Cell Carcinoma-like and Non-Small Cell Carcinoma-like Subsets. Clin Cancer Res 22: 3618–3629, 2016.
11. Laddha SV, da Silva EM, Robzyk Ket al. Integrative Genomic Characterization Identifies Molecular Subtypes of Lung Carcinoids. Cancer Res 79: 4339–4347, 2019.
12. George J, Walter V, Peifer Met al. Integrative genomic profiling of large-cell neuroendocrine carcinomas reveals distinct subtypes of high-grade neuroendocrine lung tumors. Nat Commun 9: 1048, 2018.
13. Sazonova O, Manem V, Orain Met al. Transcriptomic data helps refining classification of pulmonary carcinoid tumors with increased mitotic counts. Mod Pathol 33: 1712–1721, 2020.
14. Milione M, Maisonneuve P, Grillo Fet al. Ki-67 Index of 55% Distinguishes Two Groups of Bronchopulmonary Pure and Composite Large Cell Neuroendocrine Carcinomas with Distinct Prognosis. Neuroendocrinology 111: 475–489, 2021.
15. Alcala N, Leblay N, Gabriel AAGet al. Integrative and comparative genomic analyses identify clinically relevant pulmonary carcinoid groups and unveil the supra-carcinoids. Nat Commun 10: 3407, 2019.
16. Pelosi G, Melocchi V, Dama Eet al. An in-silico analysis reveals further evidence of an aggressive subset of lung carcinoids sharing molecular features of high-grade neuroendocrine neoplasms. Exp Mol Pathol 135: 104882, 2024.
17. Wang M, Zhao J, Zhang Let al. Role of tumor microenvironment in tumorigenesis. J Cancer 8: 761–773, 2017.
18. Klemm F, Joyce JA Microenvironmental regulation of therapeutic response in cancer. Trends Cell Biol 25: 198–213, 2015.
19. Hendry S, Salgado R, Gevaert Tet al. Assessing Tumor-Infiltrating Lymphocytes in Solid Tumors: A Practical Review for Pathologists and Proposal for a Standardized Method from the International Immuno-Oncology Biomarkers Working Group: Part 2: TILs in Melanoma, Gastrointestinal Tract Carcinomas, Non-Small Cell Lung Carcinoma and Mesothelioma, Endometrial and Ovarian Carcinomas, Squamous Cell Carcinoma of the Head and Neck, Genitourinary Carcinomas, and Primary Brain Tumors. Adv Anat Pathol 24: 311–335, 2017.
20. Sarnaik AA, Hwu P, Mule JJ, Pilon-Thomas S Tumor-infiltrating lymphocytes: A new hope. Cancer Cell 42: 1315–1318, 2024.
21. Chen Z, Lin S, Liang Fet al. The prognostic and therapeutic value of the tumor microenvironment and immune checkpoints in pancreatic neuroendocrine neoplasms. Sci Rep 14: 24669, 2024.
22. Werner W, Detjen K, Bruneau Aet al. Intratumoral dendritic cells and T cells predict survival in gastroenteropancreatic neuroendocrine neoplasms. Endocr Relat Cancer 30, 2023.
23. Centonze G, Lagano V, Sabella Get al. Myeloid and T-Cell Microenvironment Immune Features Identify Two Prognostic Sub-Groups in High-Grade Gastroenteropancreatic Neuroendocrine Neoplasms. J Clin Med 10, 2021.
24. Baretti M, Zhu Q, Zahurak Met al. Prognostic Implications of the Immune Tumor Microenvironment in Patients With Pancreatic and Gastrointestinal Neuroendocrine Tumors. Pancreas 50: 719–726, 2021.
25. Milione M, Miceli R, Barretta Fet al. Microenvironment and tumor inflammatory features improve prognostic prediction in gastro-entero-pancreatic neuroendocrine neoplasms. J Pathol Clin Res 5: 217–226, 2019.
26. Wang H, Li Z, Dong Bet al. Prognostic significance of PD-L1 expression and CD8+ T cell infiltration in pulmonary neuroendocrine tumors. Diagn Pathol 13: 30, 2018.
27. Niedra H, Peculis R, Saksis Ret al. Tumor and alpha-SMA-expressing stromal cells in pancreatic neuroendocrine tumors have a distinct RNA profile depending on tumor grade. Mol Oncol 19: 659–681, 2025.
28. Centonze G, Maisonneuve P, Simbolo Met al. Ascl1 and OTP tumour expressions are associated with disease-free survival in lung atypical carcinoids. Histopathology 82: 870–884, 2023.
29. Herbst RS, Baas P, Kim DWet al. Pembrolizumab versus docetaxel for previously treated, PD-L1-positive, advanced non-small-cell lung cancer (KEYNOTE-010): a randomised controlled trial. Lancet 387: 1540–1550, 2016.
30. Petersen I, Dietel M, Geilenkeuser WJ et al. EGFR immunohistochemistry as biomarker for antibody-based therapy of squamous NSCLC - Experience from the first ring trial of the German Quality Assurance Initiative for Pathology (QuIP((R))). Pathol Res Pract 213: 1530–1535, 2017.

31. Yoo SY, Park HE, Kim JHet al. Whole-Slide Image Analysis Reveals Quantitative Landscape of Tumor-Immune Microenvironment in Colorectal Cancers. Clin Cancer Res 26: 870–881, 2020.
32. Bankhead P, Loughrey MB, Fernandez JAet al. QuPath: Open source software for digital pathology image analysis. Sci Rep 7: 16878, 2017.
33. Kursa MB, Rudnicki WR Feature Selection with the Boruta Package. Journal of Statistical Software 36: 1 – 13, 2010.
34. Yan F, Chen X, Quan X, Wang L, Wei X, Zhu J Association between the stress hyperglycemia ratio and 28-day all-cause mortality in critically ill patients with sepsis: a retrospective cohort study and predictive model establishment based on machine learning. Cardiovasc Diabetol 23: 163, 2024.
35. Ferencz B, Megyesfalvi Z, Csende Ket al. Comparative expression analysis of immune-related markers in surgically resected lung neuroendocrine neoplasms. Lung Cancer 181: 107263, 2023.
36. Tsuruoka K, Horinouchi H, Goto Yet al. PD-L1 expression in neuroendocrine tumors of the lung. Lung Cancer 108: 115–120, 2017.
37. Vesterinen T, Kuopio T, Ahtiainen Met al. PD-1 and PD-L1 expression in pulmonary carcinoid tumors and their association to tumor spread. Endocr Connect 8: 1168–1175, 2019.
38. Kasajima A, Ishikawa Y, Iwata Aet al. Inflammation and PD-L1 expression in pulmonary neuroendocrine tumors. Endocr Relat Cancer 25: 339–350, 2018.
39. Simbolo M, Barbi S, Fassan Met al. Gene Expression Profiling of Lung Atypical Carcinoids and Large Cell Neuroendocrine Carcinomas Identifies Three Transcriptomic Subtypes with Specific Genomic Alterations. J Thorac Oncol 14: 1651–1661, 2019.

Authors and Affiliations

Giovanni Centonze[1,2] · Patrick Maisonneuve[3] · Émilie Mathian[4] · Federica Grillo[5] · Giovanna Sabella[1] · Vincenzo Lagano[1] · Alessandro Mangogna[6] · Sara Pusceddu[7] · Paola Bossi[8] · Paola Spaggiari[8] · Alessandro Del Gobbo[9] · Stefano Ferrero[9] · Luigi Rolli[10] · Ugo Pastorino[10] · Luisa Bercich[11] · Andrea Tironi[11] · Mauro Roberto Benvenuti[12] · Maria Sole Gallazzi[12] · Rosalia Romano[12] · Alfredo Berruti[13] · Luca Roz[14] · Carlo Capella[15] · Matthieu Foll[4] · Massimo Milione[1]

✉ Massimo Milione
massimo.milione@istitutotumori.mi.it

[1] 1 st Pathology Division, Department of Pathology and Laboratory Medicine, Fondazione IRCCS Istituto Nazionale dei Tumori, Milan, Italy

[2] Food Safety and Nutrition Service (S.I.A.N.) - Department of Prevention, Azienda Sanitaria Locale CN2, Alba-Bra, Italy

[3] Division of Epidemiology and Biostatistics, European Institute of Oncology (IEO) IRCCS, Milan, Italy

[4] Computational Cancer Genomics Team, Genomic Epidemiology Branch (GEM), International Agency for Research on Cancer/World Health Organization (IARC/WHO), Lyon, France

[5] Unit of Pathology, Department of Surgical Sciences and Integrated Diagnostics, University of Genoa and Ospedale Policlinico San Martino, Genoa, Italy

[6] Institute of Pathological Anatomy, Department of Medicine, University of Udine, Udine, Italy

[7] Medical Oncology Department, Fondazione IRCCS, Istituto Nazionale dei Tumori, Milan, Italy

[8] Pathology Department, Humanitas Clinical and Research Center, Humanitas Milan ENETS Center of Excellence, Milan, Italy

[9] Division of Pathology, Fondazione IRCCS Ca' Granda Ospedale Maggiore Policlinico, Milan, Italy

[10] Thoracic Surgery Unit, Fondazione IRCCS Istituto Nazionale Tumori, Milan, Italy

[11] Department of Pathology, ASST Spedali Civili of Brescia, Brescia, Italy

[12] Thoracic Surgery Unit, Department of Medical and Surgical Specialties Radiological Sciences and Public Health, Medical Oncology, University of Brescia, ASST Spedali Civili of Brescia, Brescia, Italy

[13] Medical Oncology Unit, ASST Spedali Civili of Brescia, Department of Medical and Surgical Specialties, Radiological Science and Public Health, University of Brescia, Brescia, Italy

[14] Epigenomics and Biomarkers of Solid Tumors , Fondazione IRCCS Istituto Nazionale dei Tumori, Milano, Italy

[15] Department of Medicine and Surgery, University of Insubria, Varese, Italy